drones

MDPI

*Article*

# A Cooperative UAV Hyperspectral Imaging and USV In Situ Sampling Framework for Rapid Chlorophyll-*a* Retrieval

**Zixiang Ye, Xuewen Chen, Lvxin Qian, Chaojun Lin and Wenbin Pan ***

College of Environment & Safety Engineering, Fuzhou University, Fuzhou 350116, China; 230627025@fzu.edu.cn (Z.Y.); 240627031@fzu.edu.cn (X.C.); 240627064@fzu.edu.cn (L.Q.); 230627044@fzu.edu.cn (C.L.)

* Correspondence: wenbinpan@fzu.edu.cn

## Highlights

### What are the main findings?

- The study demonstrated that the integration of UAV hyperspectral imaging with USV in situ sampling enables the rapid and accurate assessment of Chl-*a* concentrations. This collaborative framework provides real-time, fine-scale Chl-*a* mapping and offers a promising solution for emergency monitoring of water quality in small inland water bodies, such as drinking-water reservoirs.
- A two-stage feature selection strategy and four machine learning models were evaluated, with the Random Forest (RF) model achieving the highest accuracy and robustness, particularly under small-sample conditions. This highlights the RF model's ability to provide reliable Chl-*a* estimation even when data availability is limited.

### What are the implications of the main findings?

- The framework provides a rapid-deployment technical pathway for emergency water-quality assessment, especially for algal bloom response in small inland drinking-water sources.
- The proposed workflow enhances the ground–aerial segment of integrated monitoring networks, supporting real-time decision-making and scalable applications in future UAV-based environmental surveillance.

## Abstract

Traditional water quality monitoring methods are limited in providing timely chlorophyll-*a* (Chl-*a*) assessments in small inland reservoirs. This study presents a rapid Chl-*a* retrieval approach based on a cooperative unmanned aerial vehicle–uncrewed surface vessel (UAV–USV) framework that integrates UAV hyperspectral imaging, machine learning algorithms, and synchronized USV in situ sampling. We carried out a three-day cooperative monitoring campaign in the Longhu Reservoir of Fujian Province, during which high-frequency hyperspectral imagery and water samples were collected. An innovative median-based correction method was developed to suppress striping noise in UAV hyperspectral data, and a two-step band selection strategy combining correlation analysis and variance inflation factor screening was used to determine the input features for the subsequent inversion models. Four commonly used machine-learning-based inversion models were constructed and evaluated, with the random forest model achieving the highest accuracy and stability across both training and testing datasets. The generated Chl-*a* maps revealed overall good water quality, with localized higher concentrations in weakly hydrodynamic zones. Overall, the cooperative UAV–USV framework enables synchronized

Check for updates

Academic Editor: David R. Green

Received: 18 November 2025
Revised: 25 December 2025
Accepted: 5 January 2026
Published: 7 January 2026

**Copyright:** © 2026 by the authors. Licensee MDPI, Basel, Switzerland. This article is an open access article distributed under the terms and conditions of the Creative Commons Attribution (CC BY) license.

data acquisition, rapid processing, and fine-scale mapping, demonstrating strong potential for fast-response and emergency water-quality monitoring in small inland drinking-water reservoirs.

**Keywords:** UAV hyperspectral images; water quality; chlorophyll a concentration; emergency monitoring

## 1. Introduction

Inland aquatic ecosystems play a crucial role in supporting human well-being, providing ecosystem services that encompass multiple aspects, including the supply of drinking water resources [1]. However, these water bodies face multiple anthropogenic pressures, including climate change, and are under severe threat globally [2,3]. Phytoplankton abundance is a key indicator of the trophic status and water quality of inland waters [4]. In recent decades, the intensification of eutrophication coupled with global warming has substantially increased the frequency and severity of phytoplankton blooms [5,6]. The increase in occurrence of harmful algal blooms has disrupted water quality and ecological stability in many inland water systems [7,8]. Therefore, the capability to rigorously monitor and accurately quantify phytoplankton dynamics is of critical importance for protecting aquatic ecosystems and sustaining human well-being.

Chlorophyll-*a* (Chl-*a*) is ubiquitously present in phytoplankton and is therefore widely used as a proxy for phytoplankton biomass [9,10]. It serves as a fundamental parameter in aquatic ecology, environmental monitoring, and water resource management [11]. Traditionally, in situ sampling provides accurate measurements of water quality parameters at specific sampling sites. However, such methods are time-consuming, labor-intensive, and costly, thereby limiting their applicability for large-scale monitoring [12,13]. With the advantages of broad spatial coverage and continuous temporal observation, remote sensing technology has gradually become a mainstream approach for characterizing the spatial distribution and temporal dynamics of water quality constituents [14,15]. Common satellite sensors used for the remote estimation of Chl-*a* concentration include the Ocean and Land Colour Instrument (OLCI), the Medium Resolution Imaging Spectrometer (MERIS), Landsat TM/ETM+/OLI, and the Moderate Resolution Imaging Spectroradiometer (MODIS) [16].

Nevertheless, the vertical and horizontal migration of phytoplankton is influenced by factors such as light conditions and hydrological dynamics, causing Chl-*a* concentrations to fluctuate significantly over the course of a day or even within a few hours [17,18]. Spaceborne remote sensing is constrained by satellite revisit cycles and cloud contamination, resulting in limited availability of high-quality imagery that can capture the rapid spatiotemporal variations in phytoplankton blooms in inland waters [19]. Previous studies have reported that in some regions, only about 24% of Landsat images acquired throughout the year are usable, and from April to July—the peak bloom period—clear images are almost unavailable [20]. Consequently, satellite-based remote sensing cannot always provide timely and accurate water quality information due to factors such as cloud cover, precipitation, and relatively coarse spatial resolution [21,22]. This limitation is particularly critical for locally sensitive areas, such as drinking-water sources, where real-time or emergency monitoring is required.

Unmanned aerial vehicle (UAV) remote sensing, characterized by high spatial–temporal resolution and flexible image acquisition, provides an efficient and cost-effective means for monitoring the water quality of small and medium-sized inland water bodies such as lakes, rivers, and reservoirs [23]. By bridging the gap between ground-based

sampling and satellite observations, UAV remote sensing enables detailed spatial characterization and timely assessment of water quality dynamics, thereby supporting precise water management and pollution control efforts [24,25]. In recent years, numerous studies have utilized UAV systems to investigate phytoplankton dynamics in small inland waters. UAV platforms equipped with RGB, multispectral, or hyperspectral sensors have been successfully employed to retrieve Chl-*a* concentrations in various aquatic environments [26]. Among these, hyperspectral sensors—owing to their satisfactory spectral resolution on the order of several nanometers—have demonstrated superior accuracy in water quality retrieval, particularly in complex inland water systems [27,28].

UAVs have been widely applied in various emergency monitoring scenarios. However, most existing studies focus on geological disasters, wildfires, and floods, while relatively few have addressed water quality or algal bloom emergencies [29,30]. Algal bloom emergency monitoring refers to a rapid-response environmental procedure initiated when a sudden bloom occurs or when early signs suggest an impending outbreak. This type of monitoring requires a quick assessment of bloom distribution in key areas within a limited timeframe. It enables rapid response, real-time tracking, and scientific risk evaluation, providing essential data support for subsequent warning, management, and mitigation actions. UAVs are particularly well-suited for this purpose. Their ability to operate flexibly at low altitudes allows them to capture high-spatial-resolution images at appropriate temporal frequencies. These advantages make UAV-based remote sensing one of the most effective tools for emergency monitoring of inland water quality and algal bloom events. Nevertheless, UAV imagery alone cannot accurately quantify water quality parameters without temporally matched in situ sampling data. Moreover, the use of conventional manned sampling vessels is restricted in some protected drinking-water source areas. In this context, integrating UAV remote sensing with uncrewed surface vessel (USV)-based in situ sampling becomes essential. USVs can be remotely operated to collect water samples in protected, hazardous, or otherwise inaccessible areas while minimizing disturbance to sensitive aquatic environments. When combined with UAV remote sensing, the UAV–USV framework enables near-synchronous acquisition of hyperspectral imagery and in situ water quality measurements. By improving model calibration under small-sample conditions, the integration of UAV-based remote sensing with synchronized USV sampling enhances the reliability of rapid Chl-*a* assessment, thereby providing an effective technical solution for emergency monitoring of inland algal bloom events.

The emergence of artificial intelligence (AI) technologies has significantly transformed water quality monitoring using remote sensing data. These data-driven approaches are capable of processing large volumes of data and capturing the complex nonlinear relationships between remote sensing signals and water quality parameters [31,32]. As a core branch of AI, machine learning has been widely employed for the retrieval of Chl-*a* concentration in water bodies. For instance, in irrigation ponds located in Higashihiroshima, Japan, the iterative stepwise elimination partial least squares (ISE–PLS) regression method was used to retrieve Chl-*a* and total suspended solids [33]. In a case study in Hong Kong, researchers employed multiple machine learning algorithms to estimate the concentrations of suspended solids, Chl-*a*, and turbidity [34]. In Hubei Province, UAV-based high-frequency hyperspectral observations of typical inland waters were used to construct a Chl-*a* retrieval model using XGBoost combined with feature selection techniques, enabling the analysis of diel variations in Chl-*a* and their driving factors [35]. Similarly, in the Maozhou River of Guangdong Province, a novel Bayesian probabilistic neural network (BPNN) was developed to quantitatively predict several water quality parameters, including phosphorus, nitrogen, chemical oxygen demand (COD), biochemical oxygen demand (BOD), and Chl-*a* [36]. This model was successfully applied to UAV-based hyperspectral imagery for

large-scale water quality monitoring and pollution source tracking, yielding interpretable and significant results. Previous studies have shown that among various machine learning algorithms for Chl-*a* retrieval, the random forest (RF) model is the most widely used, achieving an average coefficient of determination ($R^2$) of approximately 0.7 and demonstrating robust performance ($R^2 > 0.7$) on training datasets [10]. However, it is important to note that the "black-box" nature of specific AI algorithms limits their interpretability, hindering a deeper understanding of the underlying processes [37]. Furthermore, when models are overly complex or trained on limited datasets, overfitting may occur, thereby reducing their predictive performance on unseen data [38].

Therefore, this study focuses on the strategically significant Longhu Reservoir in Jinjiang, Fujian Province, as the study area and develops and validates a rapid Chl-*a* retrieval framework based on a cooperative UAV–USV hyperspectral monitoring system. First, a UAV–USV collaborative sampling scheme was designed to enable high-temporal-resolution acquisition of hyperspectral imagery and in situ Chl-*a* measurements within a three-day window. Subsequently, an efficient and practical method for correcting stripe noise in UAV hyperspectral imagery was proposed to optimize the preprocessing results. On this basis, a data-driven feature selection strategy was employed to systematically compare the retrieval performance of four machine learning models—the RF algorithm, the back propagation (BP) neural network algorithm, the particle swarm optimization-based least squares support vector machine (PSO–LSSVM) algorithm, and partial least squares (PLS) regression. The spatial distribution characteristics of Chl-*a* concentration were also analyzed. The overall objective of this study is to establish a rapid-deployment emergency monitoring framework for algal blooms by integrating UAV-based hyperspectral imagery with an unmanned sampling system and machine learning algorithms. This framework is expected to provide technical support for Chl-*a* retrieval in inland waters and contribute to the development of an integrated ground–aerial–space water environment monitoring network.

## 2. Materials and Methods

### 2.1. Study Area

Longhu Reservoir is located in the southeastern coastal area of Jinjiang City, Fujian Province, China (24°37′54″–24°39′6″ N, 118°36′22″–118°37′7″ E). It is the second-largest natural freshwater lake in Fujian Province, with a surface area of approximately 1.62 $km^2$ and a total storage capacity of $4.05 \times 10^6$ $m^3$ (Figure 1). Since its initial development in the 1960s, the reservoir has undergone several rounds of expansion and reconstruction, evolving into a key hydraulic facility with multiple integrated functions in regional water resource management. It serves as a vital source for drinking water supply, agricultural irrigation, and flood regulation, benefiting nearly 300,000 residents across five surrounding towns. Notably, the Longhu Reservoir serves as the primary water source for the "Fujian-to-Kinmen Water Supply Project," which was launched in 2018. Through an undersea water transfer system, it provides a stable daily water supply to Kinmen, effectively alleviating the island's freshwater scarcity. Consequently, Longhu Reservoir plays a crucial role in ensuring water security, promoting coordinated ecological governance, and fostering socio-economic connectivity across the Taiwan Strait.

### 2.2. Data Processing Workflow

The research framework is illustrated in Figure 2. First, a hyperspectral sensor mounted on a UAV was used to acquire the spectral information of the water surface. At the same time, a USV was employed to collect in situ water samples (see Section 2.3). Subsequently, the preprocessing workflow of the hyperspectral data was described (see

Section 2.4), resulting in UAV-derived hyperspectral imagery of the study area and the extraction of spectral information corresponding to the water sampling sites. Finally, feature selection and water quality retrieval modeling were performed in Section 2.5. The retrieval performance of four machine learning algorithms was evaluated in Section 3.4, and a spatial distribution map of Chl-*a* concentration was generated and analyzed in Section 3.5.

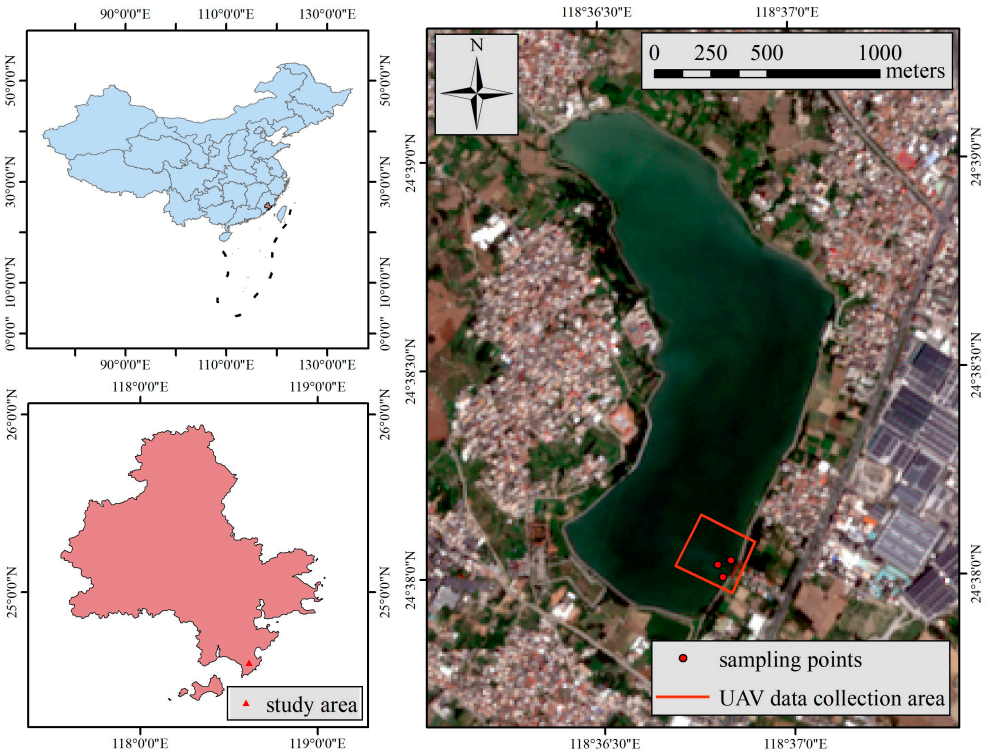


**Figure 1.** UAV data collection area and sampling points at Longhu Reservoir.

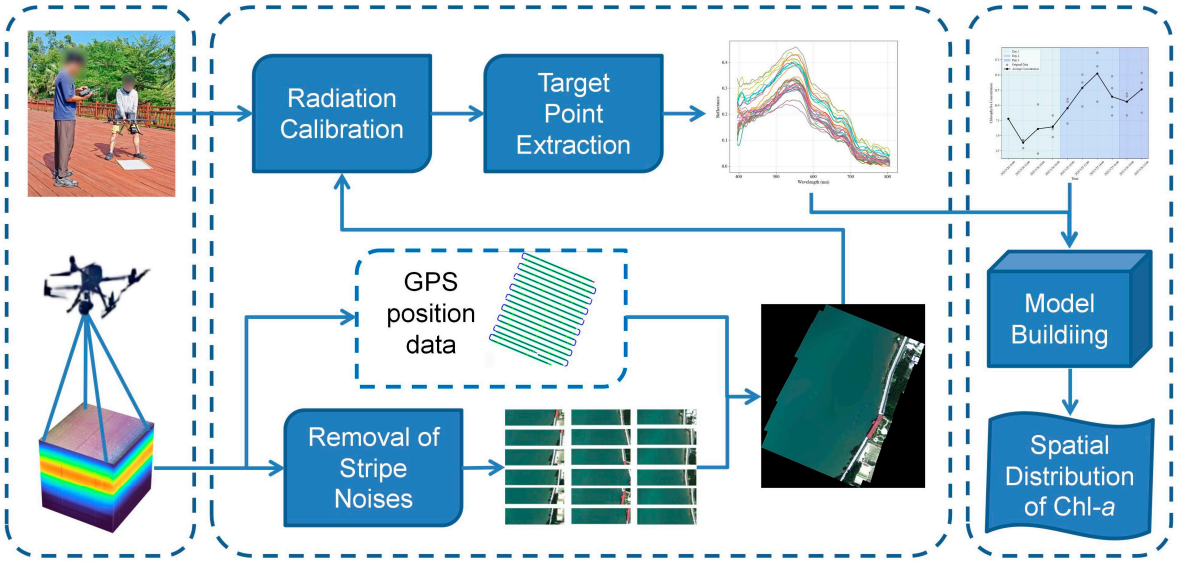


**Figure 2.** Data processing flow chart.

### *2.3. Data Collection*

#### 2.3.1. Sampling Design

The data collection was conducted from 24 to 26 March 2025, utilizing a UAV–USV collaborative operation mode to acquire hyperspectral remote sensing imagery synchronously and in situ water quality parameters within the study area. During the entire synchronized

sampling campaign, field conditions imposed certain constraints—most notably, strong winds on the afternoon of the third day. Consequently, 30 valid paired datasets comprising UAV-based hyperspectral imagery and in situ Chl-*a* concentration measurements were successfully acquired. These paired datasets formed a reliable basis for the subsequent modeling and analytical procedures.

#### 2.3.2. UAV-Based Hyperspectral Data Acquisition

In this study, a DJI Matrice 350 RTK UAV was equipped with the FS60 UAV hyperspectral imaging system (Hangzhou Color Spectrum Technology Co., Ltd., Hangzhou, China). The system integrates an embedded data acquisition and processing unit, a wireless image transmission module, and a GPS–RTK navigation system. When the RTK positioning system is functioning properly, the horizontal positioning accuracy can reach 1 cm + 1 ppm, ensuring high precision for ground sampling correspondence. The sensor covers a spectral range of 400–1000 nm with a spectral resolution of 2.5 nm and a signal-to-noise ratio of 600:1. The UAV operated at a flight altitude of 200 m, covering approximately 0.5 $km^2$ per flight. The ground sampling distance (GSD) was 18.83 cm, and the flight speed was maintained at 6.2 m/s. To ensure adequate image mosaicking, the side overlap and forward overlap were set to 70% and 80%, respectively. Before each mission, the UAV's nose was oriented toward the sun, while the hyperspectral sensor was directed vertically downward toward the center of the reference panel. This configuration ensured that the panel fully occupied the sensor's field of view, eliminating shadows and allowing for accurate exposure calibration of the hyperspectral sensor. The reference panel was then placed on an open, shadow-free ground surface within the UAV's flight area to ensure a consistent reflectance reference during data collection.

The UAV hyperspectral data acquisition followed a rigorously designed spatiotemporal sampling scheme over the selected study period. Spatially, the UAV flight area was centered on the Jinjiang–Kinmen Water Supply Project intake and extended to cover part of the lake's central region (Figure 1). This design offered two advantages: (1) it directly supported water quality monitoring and assessment at the water supply intake, and (2) it introduced partial terrestrial features (e.g., buildings) as tie points in the imagery, effectively mitigating image stitching challenges caused by homogeneous water surfaces and thereby improving the accuracy of subsequent data processing. Temporally, the UAV hyperspectral data collection followed the logistical framework [39]. In accordance with the illumination requirements of UAV-based remote sensing (solar elevation angle > 35°) and considering the UAV's battery endurance (approximately 20 min), data were repeatedly acquired at 10:00, 12:00, 14:00, and 16:00 each day to ensure sufficient temporal coverage.

#### 2.3.3. USV In Situ Sampling

Due to the protective restrictions in the Longhu Reservoir study area, manual boat-based sampling was not permitted. Therefore, a modified uncrewed surface vessel was employed to perform remote sampling operations from the shore. Three sampling sites were evenly distributed across the study area for in situ water collection. During the ten UAV hyperspectral data acquisition periods, the USV simultaneously conducted in situ water quality sampling. The USV was equipped with an 18,000 mAh battery and a GPS positioning module, ensuring sufficient endurance and positional accuracy during sampling. Powered by dual 12 V motors, it had a maximum control range of 500 m, which adequately covered the sampling area and ensured high sampling efficiency. A release system was mounted at the rear of the USV to deploy the water sampler upon remote command. By adjusting the length of the tether, water samples were collected at a depth of 0.5 m. During navigation, the pressure of the surrounding water effectively

prevented mixing with other water layers, thereby maintaining the representativeness of the collected samples (Figure 3). After collection, the water samples were stored refrigerated in the dark and filtered on the same day onto glass fiber filter pads. The filter pads were immediately frozen after filtration and transported to the laboratory in a single batch after the completion of all field sampling. Chl-*a* concentrations were determined using the ethanol spectrophotometric method [40].



**Figure 3.** Posture of the USV water sampler before and after deployment, and collection of water samples.

Each sampling round trip required approximately 5 min, and the sampling time was precisely synchronized with the UAV hyperspectral data acquisition, with a time deviation controlled within 5 min. Such synchronization ensured temporal consistency between the water samples and the hyperspectral imagery. Additionally, the modified USV measured only 0.55 m × 0.32 m, and its relatively small top-view area ensured negligible interference with UAV imaging. Consequently, this method enabled fully synchronized acquisition of water samples and UAV hyperspectral data, significantly enhancing the spatiotemporal correspondence between the two datasets.

### *2.4. Hyperspectral Data Processing*

The workflow of UAV-based hyperspectral data processing is illustrated in Figure 2. After acquiring the raw hyperspectral stripes, stripe noise removal was first performed for each flight strip. Stripe noise is a common type of systematic noise in UAV hyperspectral imagery. It typically appears as a gradual attenuation of radiance values toward the image edges, resulting in radiometric non-uniformity along the flight direction and noticeable vignetting effects near the boundaries [41]. The degree of stripe noise varies among spectral bands (Figure 4), which may be attributed to the inconsistent response of detector elements in the imaging sensor. The presence of stripe noise significantly reduces the signal-to-noise ratio of hyperspectral data, compromising both radiometric uniformity and geometric mosaicking accuracy. Consequently, it can lead to radiometric discontinuities along mosaic seams. More importantly, stripe noise introduces spectral fluctuations, reducing the smoothness and continuity of spectral curves. These fluctuations, in turn, affect the identification and extraction of spectral features, ultimately decreasing the accuracy of Chl-*a* retrieval.

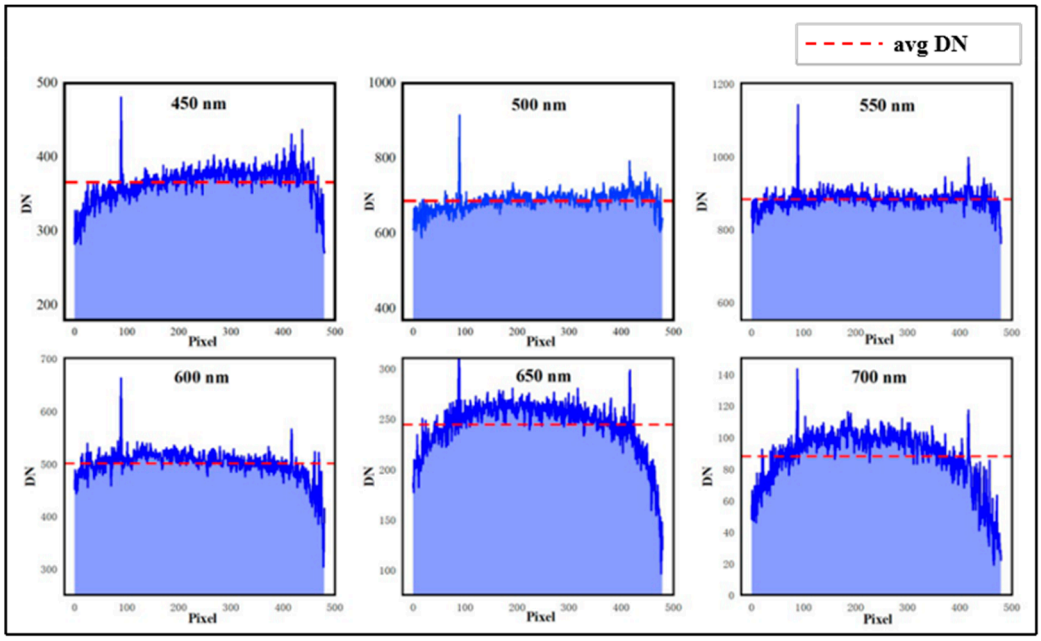


**Figure 4.** Stripe noise in different frequency bands.

Stripe noise removal was conducted based on the spatial distribution characteristics of the noise. Since such noise primarily occurs along the direction perpendicular to the UAV's flight path, pixels within the same column exhibit nearly identical radiometric attenuation. Therefore, the central column of the image was regarded as a reference, assuming it was unaffected by attenuation. On this basis, it was assumed that the water body substrate remained spatially homogeneous, implying that pixels in different columns should have similar radiometric median values [42]. By comparing the radiometric differences between each column and the reference column, and subsequently applying corrections to the affected columns, the stripe artifacts caused by radiometric attenuation were effectively eliminated (Equation (1)):

$$DN_{corrected(x,y,i)} = DN_{(x,y,i)} + \left(Median_{refer(i)} - Median_{(x,i)}\right) \quad (1)$$

where $Median_{refer(i)}$ represents the median DN value of the pixels in the central column of band i. In this study, each UAV flight strip contained 480 pixels in width; therefore, the 240th column was selected as the reference column. $Median_{(x,i)}$ represents the median value of the column containing the current pixel.

After completing the stripe correction, the flight line cropping and image mosaicking were performed using FigSpec Merge (v1.25.4.16) software, developed by Hangzhou Caipu Technology Co., Ltd. (Hangzhou, China). The cropping ratio for the upper and lower edges was set to 0.2, and a feature-based mosaicking algorithm was employed. This method effectively identifies and registers common points between adjacent flight lines, thereby improving both mosaicking accuracy and geometric consistency. During the image mosaicking, FigSpec Merge automatically matched the hyperspectral data acquired by the UAV with the simultaneously recorded GPS positioning information, ultimately generating georeferenced hyperspectral images. These images were spatially aligned with the field sample points collected by the USV. Subsequently, the generated hyperspectral images underwent radiometric correction using FigSpec Studio 2.0, also developed by Hangzhou Caipu Technology Co., Ltd. The correction was based on a gray reference panel with known reflectance values, deployed on the ground, which converted the sensor-acquired dimensionless raw radiance values into actual reflectance. This step eliminated radiometric

distortions caused by sensor response differences and variations in illumination conditions. Considering the flight altitude of 200 m, the atmospheric path was relatively short, and complex interferences such as atmospheric scattering and absorption had a minimal effect on radiative transfer [43]. Therefore, no atmospheric correction was applied in this study.

### *2.5. Model Development*

#### 2.5.1. Spectral Feature Selection

UAV-based hyperspectral data provide abundant information about water bodies. However, when retrieving Chl-*a* concentration directly from the raw single-band reflectance, it is easily affected by high concentrations of suspended sediments (SS) and aquatic vegetation, resulting in weak correlations between single-band reflectance and Chl-*a* concentration [44]. Constructing spectral indices through band combinations is an effective approach to enhance the spectral contrast between the target and the background [45]. In this study, all possible band combinations were exhaustively computed based on the traditional three-band index strategy, and the existing empirical algorithms were also computed (Table 1) [46].

**Table 1.** Existing empirical algorithms for Chl-*a* concentration inversion.

| Number | Algorithm | Equation | Reference |
|---|---|---|---|
| 1 | NDCI | $(R_{708} - R_{665})/(R_{708} + R_{665})$ | [47] |
| 2 | INDEX | $\left(R_{665}^{-1} - R_{708}^{-1}\right)/\left(R_{753}^{-1} - R_{708}^{-1}\right)$ | [48] |
| 3 | KIVU | $(R_{459} - R_{644})/R_{530}$ | [49] |
| 4 | G2B | $R_{708}/R_{665}$ | [50] |
| 5 | NGBDI | $(R_{560} - R_{482})/(R_{560} + R_{482})$ | [51] |
| 6 | NGRDI | $(R_{560} - R_{665})/(R_{560} + R_{665})$ | [52] |
| 7 | SABI | $(R_{857} - R_{644})/(R_{459} + R_{530})$ | [53] |

While hyperspectral data provide abundant spectral information, the strong information redundancy and multicollinearity among bands present significant challenges for machine learning modeling. Such redundant features not only fail to enhance model performance but also interfere with the training process, increase the risk of overfitting, and weaken model robustness and interpretability. Therefore, feature selection is a critical step in constructing efficient and reliable retrieval models for hyperspectral data analysis. According to different feature evaluation strategies, common feature selection methods can be categorized into three types: filter methods, embedded methods, and wrapper methods [54]. The Pearson correlation coefficient method is a typical filter-based approach. It is simple in principle and computationally efficient, and has been widely used in previous studies for preliminary screening of features with high correlation to the target variable. However, this method only assesses the strength of association between variables and the response and cannot identify or eliminate multicollinearity within the feature set [55]. The variance inflation factor (VIF), a commonly used collinearity diagnostic index, can effectively quantify the degree of linear overlap between features. It is often employed to remove highly collinear variables before model construction, thereby improving model stability and interpretability. In this study, to balance feature relevance, quantity, and independence, a two-stage feature selection strategy was adopted. First, based on the correlation coefficient method, all possible spectral indices were screened, and those with an absolute correlation coefficient greater than 0.7 with Chl-*a* concentration were retained. This threshold was chosen to ensure that strongly correlated features were preserved while maintaining a sufficient number of candidate features for subsequent screening. To further

reduce feature dimensionality and eliminate multicollinearity, the VIF method was then applied to impose a collinearity constraint on the initially selected features.

#### 2.5.2. Machine Learning Methods

Subsequently, four machine learning models were employed to retrieve Chl-*a* concentration. The RF algorithm is an ensemble learning method that constructs a large number of decision trees and aggregates their predictions (e.g., by averaging) to enhance the model's generalization ability and robustness [56]. This model is well-suited for handling high-dimensional features and can estimate generalization error using out-of-bag samples, thereby exhibiting a certain resistance to overfitting. The BP neural network is a multilayer feed-forward neural network trained using the error back-propagation algorithm. Its structure consists of an input layer, one or more hidden layers, and an output layer. The BP neural network iteratively adjusts the connection weights between neurons through the gradient descent method to approximate complex nonlinear functions, making it particularly suitable for modeling data characterized by strong nonlinear relationships among variables. The PLS regression has been widely applied in spectral modeling. Its core principle is to extract latent variables from both independent and dependent variables that best explain their covariance structure. This approach is particularly robust when features exhibit high collinearity and the sample size is limited. The least squares support vector machine (LSSVM) is a modified version of the standard support vector machine (SVM). It replaces the traditional loss function with a least squares loss, thereby transforming the optimization process into solving a system of linear equations, which greatly improves computational efficiency. However, the performance of LSSVM is highly sensitive to its regularization and kernel parameters. To address this issue, the particle swarm optimization (PSO) algorithm was introduced in this study to perform automatic global optimization of these key parameters by simulating swarm intelligence. The hybrid model integrating PSO and LSSVM is referred to as PSO–LSSVM.

#### 2.5.3. Model Validation and Evaluation

In this study, the dataset was randomly divided using the 'train_test_split' function in Scikit-learn, with 80% of the samples allocated for training and the remaining 20% reserved for testing. Model performance was evaluated using the coefficient of determination ($R^2$), root mean squared error (RMSE), and mean absolute error (MAE):

$$R^2 = 1 - \frac{\sum_{i=1}^{n}(y_i - \hat{y}_i)^2}{\sum_{i=1}^{n}(y_i - \overline{y})^2} \quad (2)$$

$$\mathrm{RMSE} = \sqrt{\frac{1}{n}\sum_{i=1}^{n}(y_i - \hat{y}_i)^2} \quad (3)$$

$$\mathrm{MAE} = \frac{1}{n}\sum_{i=1}^{n}|y_i - \hat{y}_i| \quad (4)$$

where $y_i$ represents the measured value of the i-th sample, $\hat{y}_i$ is the corresponding predicted value, $\overline{y}$ denotes the mean of all measured values, and n is the total number of samples. A higher $R^2$ value and lower RMSE and MAE values indicate better model accuracy and predictive performance.

## 3. Results

### *3.1. De-Striping*

During the stripe correction process, to prevent sun glint interference from biasing the column-wise median estimation, a sun glint detection mechanism based on the Sun Glint

Aware Restoration (SUGAR) algorithm was incorporated [57]. Detected sun glint regions were masked to eliminate their influence on the stripe correction results. Additionally, the reference baseline for stripe correction was derived from the flight strip acquired during the middle phase of the UAV's flight mission. By applying a unified correction to all flight strips, this procedure aimed to minimize subtle variations in water-body irradiance caused by changing illumination conditions during flight.

As shown in Figure 5a, the original UAV image exhibits a noticeable brightness attenuation at the edges perpendicular to the flight direction, where the edge regions appear significantly darker than the image center. In addition, dark stripe noise of varying widths appears intermittently across the image, resulting in local distortion. From the 3D data view in Figure 5b, it can be further observed that the DN values of the water body decrease more sharply near the image edges. After processing with the median-based stripe correction method, the overall image becomes more uniform in tone, and color consistency is significantly improved (Figure 5c). The dark stripes and edge attenuation artifacts are effectively removed, and the water body features are well restored, as also verified in the 3D data view shown in Figure 5d. These results indicate that the proposed median correction approach can effectively suppress sensor-induced noise. The proposed method in this study can correct both stripe noise distribution and edge attenuation without requiring a white reference panel [41]. Compared with the structure-guided one-way transformation approach, this method avoids complex parameter tuning while substantially reducing image processing time [58].

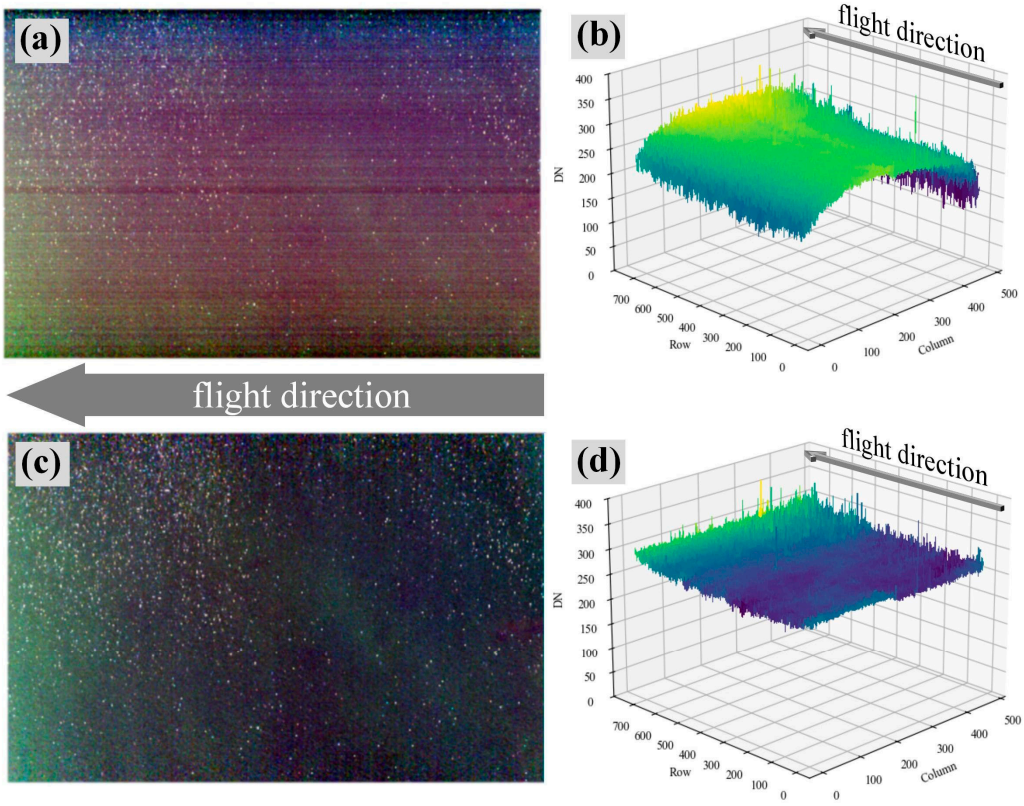


**Figure 5.** Comparison before and after strip removal. (**a**) An original image segment without strip removal. (**b**) A 3D data view of the original image segment. (**c**) The corrected image segment after strip removal. (**d**) A 3D data view of the corrected image segment.

### *3.2. Data Analysis of Longhu Reservoir Samples*

Spectral reflectance data at each sampling point were extracted from the preprocessed UAV-based hyperspectral images. Since the spectral bands beyond 800 nm approached

near-zero values, a total of 198 bands within the range of 396.05 nm to 805.15 nm were selected for spectral smoothing, and continuous spectral curves were plotted (Figure 6a). Considering that variations in illumination conditions occurred during UAV data acquisition, the original spectral reflectance values exhibited certain fluctuations. Therefore, all spectral curves were subjected to min–max normalization to facilitate visualization. After normalization, the spectral distributions became more compact, highlighting the distinctive spectral shape characteristics.

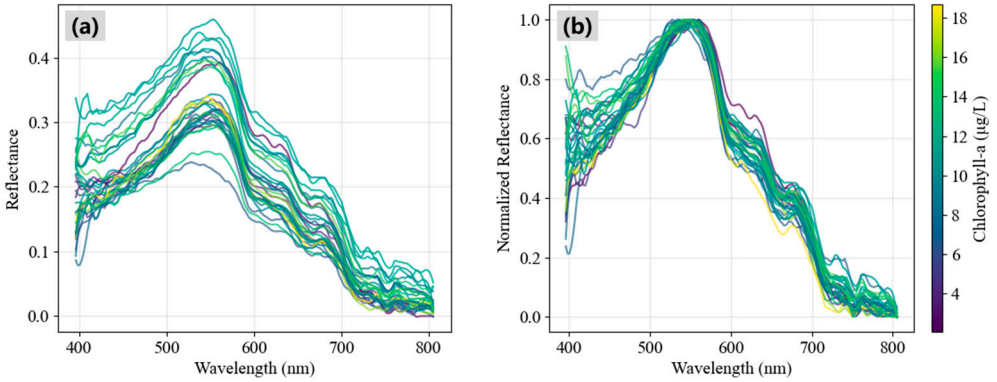


**Figure 6.** Raw spectral curve (**a**) and normalized spectral curve (**b**).

The original spectral curves exhibit an overall increasing trend in water surface reflectance within the 400–550 nm range, with a peak at approximately 550 nm. As illustrated in the normalized spectra (Figure 6b), the water body with the highest Chl-*a* concentration (yellow curve) exhibits a pronounced and steep reflectance peak in the green band. In contrast, the water body with the lowest Chl-*a* concentration (purple curve) shows a more gradual variation in reflectance across this wavelength range. Around 670 nm, all spectra display a typical red absorption trough, caused by the strong absorption of red light by Chl-*a* within phytoplankton cells. Beyond 700 nm, the spectral reflectance decreases rapidly, with two minor reflectance peaks observed at approximately 740 nm and 760 nm. Subsequently, due to strong water absorption and scattering by suspended particles, the reflectance approaches zero. Although variations existed in sampling time and spatial location, the overall spectral patterns across all sites remained consistent. The subtle differences observed in the spectral features were primarily attributed to variations in Chl-*a* concentration.

A total of 30 water samples were collected in this study, and the laboratory analysis results are shown in Figure 7. Due to field constraints, only one sample was obtained at 10:00 on 24 March 2025, which was treated as the mean value for that time period. The Chl-*a* concentrations exhibited strong spatial consistency among different sampling sites within the same observation period. However, they showed pronounced temporal heterogeneity across different time periods, with a coefficient of variation reaching 41.86%. Overall, the Chl-*a* concentration displayed a clear increasing trend during the three-day observation period. Detailed descriptive statistics are presented in Table 2.

**Table 2.** Statistical results for Chl-*a* concentration.

| n | Max (μg/L) | Min (μg/L) | Mean (μg/L) | SD (μg/L) | CV |
|---|---|---|---|---|---|
| 30 | 19 | 2 | 10 | 4 | 40% |

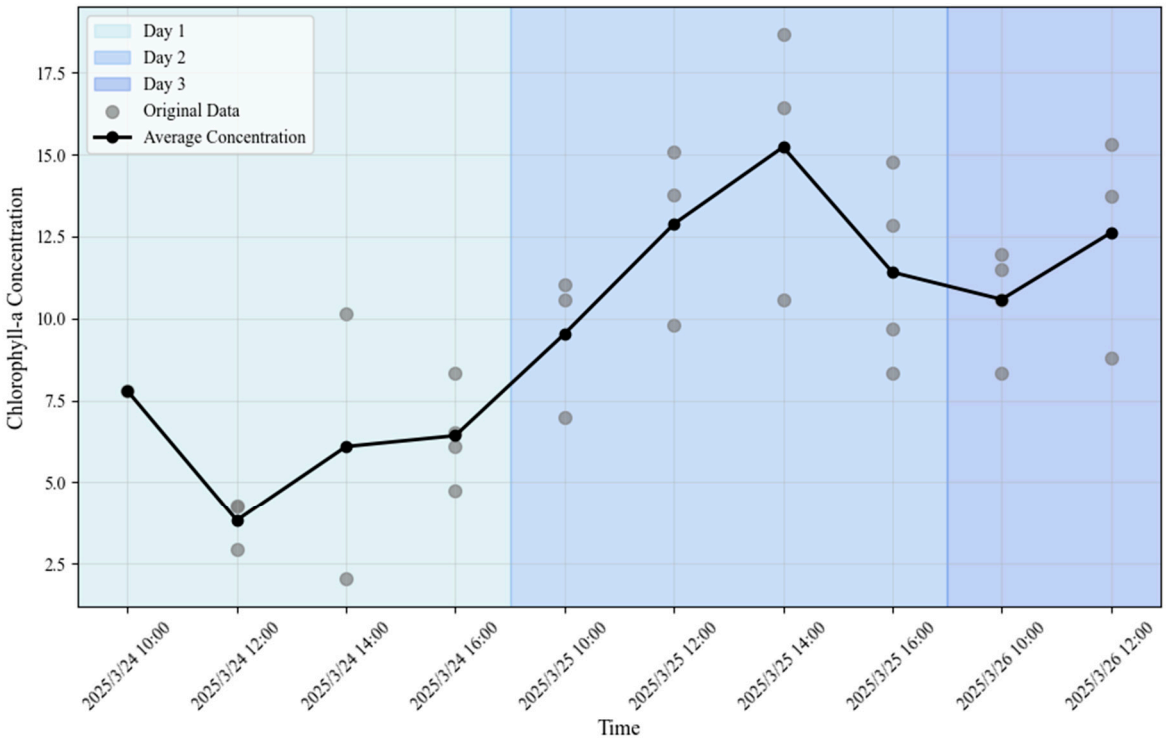


**Figure 7.** Chl-*a* concentration data for the three days from 24 March to 26 March 2025.

### *3.3. Feature Selection Results*

The correlation analysis between the original spectral reflectance and Chl-*a* concentration is illustrated in Figure 8. The analysis indicates that the correlations across most wavelengths are generally weak, with correlation coefficients ranging from 0.2 to 0.3. Such weak correlations may be attributed to residual noise and environmental influences that persisted even after radiometric correction, leading to variability in the reflectance data. The correlation curve reveals that the relationship between reflectance and Chl-*a* concentration is relatively stronger in the green band (approximately 500–600 nm) and the red-edge region (approximately 680–750 nm). The relatively strong correlation suggests that variations in Chl-*a* can be effectively captured and indicated by these spectral bands.

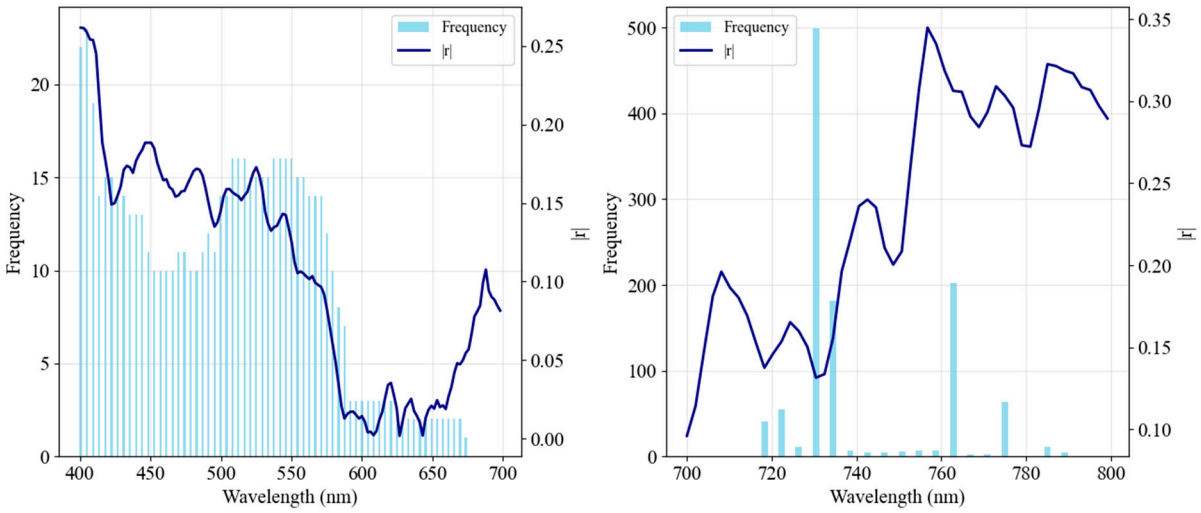


**Figure 8.** Band occurrence frequency in preferred three-band combinations and Pearson's correlation coefficients between the original spectral reflectance and Chl-*a* concentration.

Using a data-driven approach, all possible three-band combinations within the 400–800 nm range were systematically traversed and computed. A total of 1456 combinations with correlation coefficients higher than 0.7 were initially selected. The occurrence frequency of each band within these preferred combinations was then analyzed (Figure 8). The results show that in the 400–600 nm range, the frequency distribution of bands closely follows their correlation trend with Chl-*a*. In contrast, the high-frequency occurrence of bands beyond 700 nm primarily reflects the data-driven algorithm's selection of synergistic effects among specific band combinations. To further minimize multicollinearity and enhance model stability, the VIF was applied to screen these combinations, ultimately yielding nine candidate three-band indices with low redundancy. Considering both their correlation strength and optical interpretability in aquatic environments, two optimal combinations—560–732–772 nm and 531–760–732 nm—were selected as two joint input features for subsequent machine-learning modeling. These combinations not only include green wavelengths that are highly sensitive to Chl-*a* concentration in this study but also align physically with the core wavelength configurations of traditional three-band models, where bands near 730 nm and 760 nm are typically used to correct for suspended matter scattering and water absorption effects.

### *3.4. Machine Learning Results*

In this study, Chl-*a* concentration prediction models were developed using RF algorithm, BP neural network, PSO–LSSVM, PLS models. The effectiveness of these models was evaluated based on the performance metrics of the training and testing datasets (Figure 9).

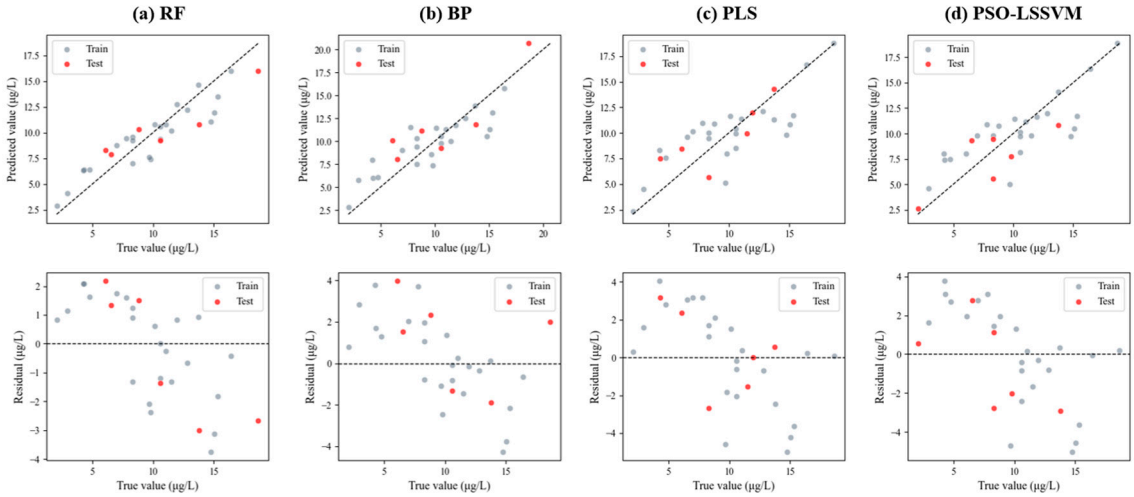


**Figure 9.** Relationship between predicted values and measured values for four machine learning models, and residual analysis plots. In the scatter plots of predicted versus measured values, the dashed line represents the 1:1 reference line indicating perfect agreement between prediction and observation. In the residual plots, the dashed line denotes the zero-residual reference line. (**a**) The RF algorithm. (**b**) The BP neural network algorithm. (**c**) The PLS algorithm. (**d**) The PSO–LSSVM algorithm.

The RF algorithm, as an ensemble learning approach, has gained widespread attention for its high training efficiency and stable predictive accuracy, particularly demonstrating strong robustness in small-sample datasets. In this study, the RF model achieved $R^2$ = 0.824, RMSE = 1.656, and MAE = 1.414 on the training set. On the testing set, the corresponding values were $R^2$ = 0.768, RMSE = 2.111, and MAE = 2.008. These results indicate that the model maintained high fitting accuracy and generalization capability during both training and testing stages, without any sign of severe overfitting. The mean residuals were close to

zero, implying that the predictions were overall unbiased, with the errors being narrowly distributed and free from systematic deviation.

In terms of parameter configuration, setting max_depth = 4 effectively constrained the growth depth of each decision tree, thereby preventing individual trees from overfitting—a crucial consideration for small-sample datasets. Although a shallower tree depth may slightly reduce the fitting capacity, it significantly enhances the model's generalization performance. Additionally, the relatively flexible settings of min_samples_split = 3 and min_samples_leaf = 1 allowed the model to capture more detailed data patterns within a limited number of samples. At the same time, the ensemble mechanism of RF helped offset the potential noise introduced by individual trees. The remarkable superiority of the RF algorithm in predicting Chl-*a* concentration from small-sample datasets in this study primarily stems from its ensemble learning strategy and intrinsic stability. Specifically, RF employs bootstrap sampling (bagging) to generate multiple decision trees and integrates their outputs, which effectively reduces model variance and mitigates the risks of overfitting in small-sample contexts.

Furthermore, the algorithm's out-of-bag error estimation mechanism enables the assessment of generalization performance without the need for an independent validation set—an essential advantage when dealing with limited data. In this study, the minor discrepancy between training and testing performance (a reduction of only 0.056 in $R^2$) further demonstrates that RF achieved a well-balanced trade-off between bias and variance through ensemble averaging, leading to improved stability and reliability under small-sample conditions. Compared with other machine learning algorithms, RF also exhibits advantages in computational efficiency and interpretability when applied to small datasets. The model's fast training speed and high accuracy are evidenced by its strong training performance ($R^2$ = 0.824) and satisfactory testing accuracy ($R^2$ = 0.768). Such results confirm that RF is a reliable and efficient approach for retrieving water quality parameters—particularly for estimating Chl-*a* concentration—when data acquisition is constrained. With its straightforward parameter tuning and consistent output, the RF model provides a robust methodological reference for subsequent studies in remote sensing-based water quality assessment.

The BP neural network, through its multilayer nonlinear transformation structure, is capable of learning the complex mapping relationships between input features and Chl-*a* concentration. The model achieved $R^2$ = 0.731, RMSE = 2.048, and MAE = 1.622 on the training set, while the testing set yielded $R^2$ = 0.715, RMSE = 2.339, and MAE = 2.172. These results indicate that the BP neural network also exhibits satisfactory fitting performance in predicting Chl-*a* concentration under small-sample conditions. Although its overall performance was slightly lower than that of the RF model, it still demonstrated considerable predictive capability. The network employed a two-hidden-layer architecture (32–16 nodes) and used the ReLU activation function to enhance nonlinear representation. A dropout mechanism (rate = 0.2) was introduced to prevent overfitting. The two-layer structure provided an appropriate model capacity under limited sample conditions, ensuring sufficient feature extraction while controlling the number of parameters. The application of the ReLU activation function effectively alleviated the vanishing gradient problem, while the dropout mechanism improved the model's generalization ability. Compared to the RF model, the primary difference between the two lies in their learning mechanisms. The BP neural network relies on gradient-descent-based global optimization, which can easily become trapped in local minima when training on small-sample datasets. In contrast, RF aggregates multiple decision trees through ensemble learning, inherently offering greater stability and resistance to overfitting.

However, in this study, the PSO–LSSVM and PLS models exhibited relatively poor performance in retrieving Chl-*a* concentration. The LSSVM model achieved $R^2$ = 0.612, RMSE = 2.538, and MAE = 2.038 on the training set, and $R^2$ = 0.600, RMSE = 2.222, and MAE = 2.034 on the testing set. Similarly, the PLS model achieved $R^2$ = 0.626, RMSE = 2.572, and MAE = 2.105 for the training set, and $R^2$ = 0.624, RMSE = 2.059, and MAE = 1.716 for the testing set. Notably, the performance of the LSSVM model was far inferior to that reported in previous studies for predicting total suspended matter ($R^2 > 0.95$). This performance degradation may be attributed to the generally low Chl-*a* concentration in the study area. Under such low-concentration conditions, both LSSVM and PLS models face significant limitations. Support vector machine-based models struggle to capture weak spectral responses associated with low concentrations of Chl-*a*. Additionally, the optical characteristics of inland and coastal waters are often complex, with suspended solids and colored dissolved organic matter (CDOM) introducing strong spectral interference. Although LSSVM employs kernel functions for nonlinear feature mapping, its capacity to disentangle mixed spectral signals is limited. Similarly, while PLS mitigates multicollinearity through principal component extraction, it still faces challenges in effectively distinguishing the spectral contributions of target parameters from those of interfering substances.

### *3.5. Inversion Results of Chl-a*

Figure 10 presents the spatial distribution of Chl-*a* concentration in the study area, retrieved from UAV hyperspectral imagery using the RF algorithm and visualized with the natural breaks classification method. The UAV images of the water body were mosaicked from multiple flight strips. Due to the limitations of the image stitching algorithm in the software developed by Hangzhou Colorspectrum Technology Co., Ltd., noticeable mosaic artifacts remain visible in the final composite image. To minimize the spatial mismatch between image pixels and in situ sampling points, a 9 × 9 spatial median filter was applied to each band independently. For each pixel, the median DN value was calculated over a 9 × 9 neighborhood of pixels in the same band. This processing effectively reduced surface reflection noise and improved the visual clarity of the retrieved Chl-*a* distribution. Additionally, some regular short-strip noise patterns are visible in the image. Their exact origin remains uncertain but is presumed to be related to either surface wave interference caused by strong winds or inherent sensor noise from the hyperspectral imaging system. Therefore, the retrieval results in this study primarily reflect the overall spatial distribution patterns of Chl-*a* concentration across the study area. The predicted value of individual pixels should not be interpreted as an accurate representation of local concentration due to residual uncertainties and potential image artifacts.

According to the retrieval results, the Chl-*a* concentration in the study area ranged from 5.83 μg/L to 16.01 μg/L, which shows good agreement with the in situ measurements (maximum 19 μg/L, minimum 2 μg/L). It is noteworthy that high Chl-*a* concentrations were mainly distributed in nearshore areas, where the retrieved values exhibited a systematic overestimation compared with field observations. Based on field survey data, this anomaly is likely closely related to the widespread presence of emergent vegetation along the shoreline. The roots and stems of emergent plants disturb bottom sediments, increasing the concentration of suspended particulates in the water and thereby enhancing scattering in the red-edge spectral region. Meanwhile, the decomposition of fallen plant material releases large amounts of dissolved organic matter, intensifying the spectral absorption effects of colored dissolved organic matter (CDOM). The combined influence of suspended matter and CDOM alters the optical properties of nearshore waters, leading to a systematic

overestimation of Chl-*a* concentrations by retrieval models constructed primarily from green and red-edge bands.

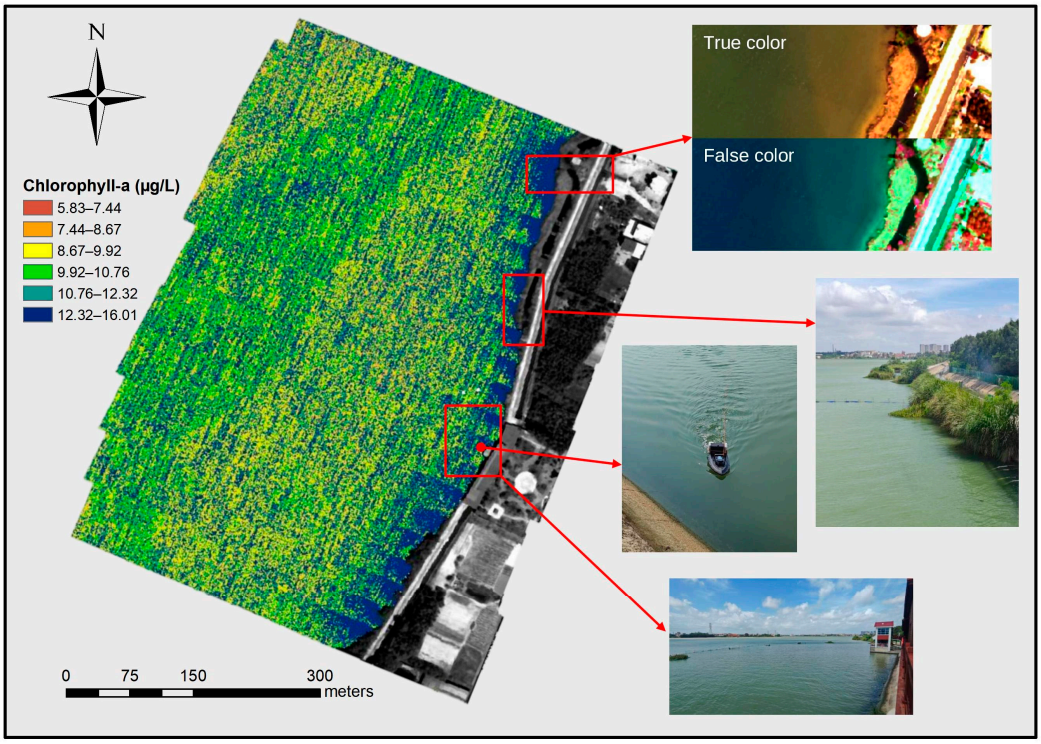


**Figure 10.** Chl-*a* retrieval results from UAV hyperspectral imagery based on the RF algorithm.

Overall, most Chl-*a* concentrations in the study area were around 10 μg/L, meeting the water quality standards for Longhu Reservoir as a drinking water source and indicating a generally good level of water cleanliness. However, a distinctly bounded anomalous patch appeared in the central area of the lake. In the retrieval map, this region is represented in green, indicating Chl-*a* concentration markedly higher than that of the surrounding waters, with a few small blue patches embedded inside representing even higher concentrations. The Chl-*a* concentration in this area was significantly higher than that in the surrounding waters. The central region of the lake is typically a weak hydrodynamic zone, characterized by low water flow velocity, limited vertical mixing, and poor water exchange capacity. Under such conditions, algal communities tend to accumulate locally, leading to a continuous increase in Chl-*a* concentration in this region. In addition, a nutrient accumulation and re-release effect may occur in the central lake area. On one hand, nitrogen, phosphorus, and other nutrients from surrounding terrestrial sources can be transported via surface runoff or groundwater toward the lake center, gradually accumulating under low-flow conditions. On the other hand, sediments at the lake bottom may release adsorbed nutrients under low-oxygen or reducing conditions, providing a sustained nutrient source for algal growth. The combined effects of these two mechanisms promote the local elevation of Chl-*a* concentration in the central region of the lake.

## 4. Discussion

The UAV–USV collaborative system, coupled with a machine learning model proposed in this study, enables the rapid and accurate retrieval of Chl-*a* concentration in a small-scale area. Although numerous studies have focused on using UAV-mounted hyperspectral sensors for retrieving inland water quality, the greater significance of this research lies in

providing a feasible emergency monitoring pathway for the development of an integrated ground–aerial–space water monitoring system for inland waters (Figure 11).

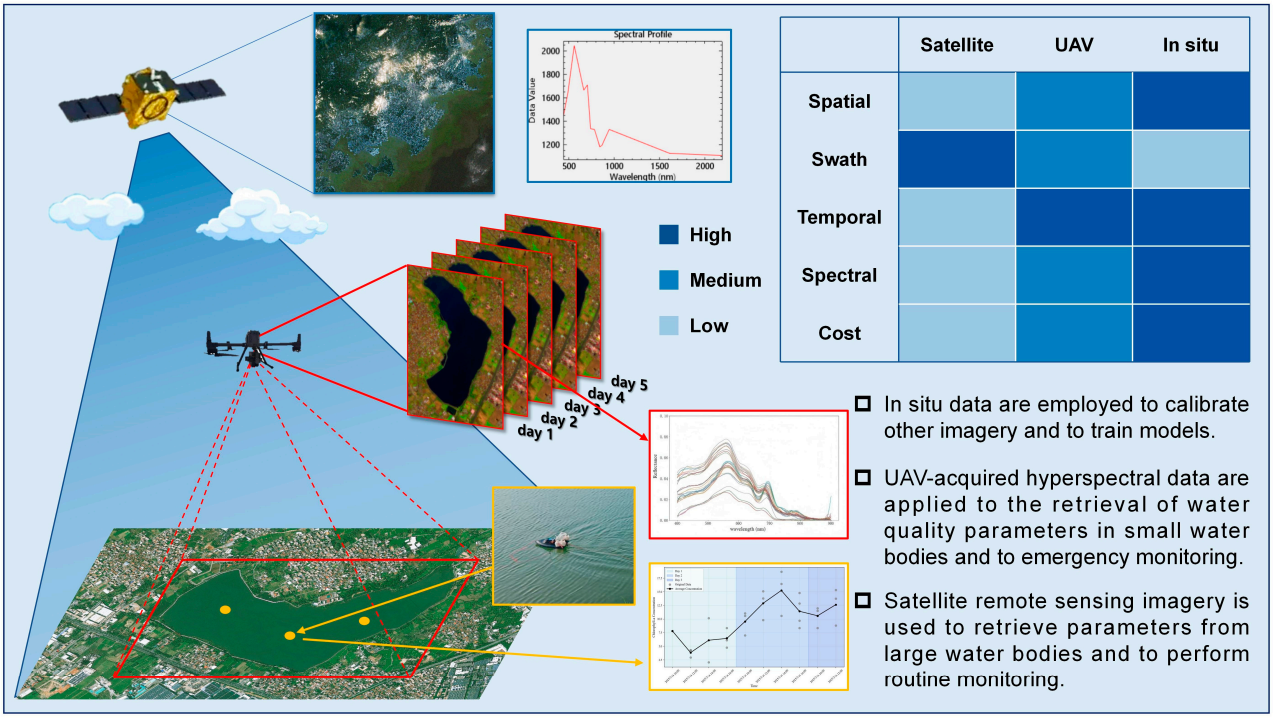


**Figure 11.** Schematic diagram of the integrated ground–aerial–space water monitoring system.

Against the backdrop of increasingly frequent eutrophication and algal bloom events, establishing an emergency monitoring system with high timeliness and precision holds significant scientific and practical value. The integrated ground–aerial–space observation system achieves full spatiotemporal coverage—from macroscopic to microscopic scales and from routine monitoring to real-time response—through the multi-tiered coordination of satellites, UAVs, and ground-based monitoring [59]. Within this framework, satellite remote sensing undertakes routine and large-scale monitoring tasks, enabling long-term tracking of water quality trends at the watershed scale. Its data are easily accessible and provide essential background information for large-scale water environment management. Ground-based monitoring, on the other hand, provides reliable calibration references for satellite and aerial retrieval results through in situ sampling and water quality measurements, thereby enhancing the generalization capability of models under varying water conditions.

In contrast, UAV-based remote sensing serves as the critical intermediary in this system. It compensates for the limited temporal resolution and revisit frequency of satellites while extending the spatial representativeness of ground-based measurements, enabling flexible, sub-meter-level regional water quality monitoring. As a result, UAV remote sensing becomes the core component of the emergency monitoring framework. The UAV–USV collaborative system developed in this study represents a practical implementation of this integrated framework. It can rapidly establish high-precision water quality models for key water areas, providing immediate data support for sudden algal bloom events.

This emergency monitoring system offers three notable advantages. First, it enables minute-level synchronized data collection between UAVs and USVs. USVs are increasingly used in water quality monitoring due to their autonomy, safety, and flexibility. Coordinating USVs with UAVs allows monitoring of areas that are difficult to access, fragile, or protected. Moreover, Chl-*a* concentrations can fluctuate significantly on an hourly scale (with a coefficient of variation of 40% in this study). If sampling and remote sensing imaging are

not synchronized, the temporal and spatial consistency of the retrieval model is directly affected. Traditional manual boat-based sampling is inefficient for large water bodies, and sampling times often differ from UAV data acquisition by several hours. By coordinating UAV and USV operations, this study not only improves sampling efficiency but also ensures that model training data are highly temporally matched, thereby guaranteeing the reliability of the retrieval results.

Second, the sampling scheme combines high efficiency with emergency responsiveness. For small water bodies, UAV docking systems can provide routine monitoring. In emergencies, UAV monitoring focuses on selected key areas, replacing traditional full-area scanning of large water bodies. This approach significantly improves operational efficiency and reduces costs while still capturing dynamic changes in algal bloom risk zones. Building on this strategy, the study successfully monitored the anomalous spatial distribution of Chl-*a* concentration at the intake of the Jinjiang–Kinmen Water Supply Project, providing a scientific foundation for water quality management in Longhu Reservoir (Figure 10).

Third, the model construction and data processing workflow are highly time-efficient, supporting rapid model development and emergency applications. During a three-day favorable weather window (with actual sampling over two and a half days), high-frequency monitoring enabled the establishment of a hyperspectral retrieval model for Chl-*a*. The results can be directly applied to real emergency scenarios. Even when suitable observation days are limited, sufficient data can be obtained to reflect the spatial distribution of water quality parameters, providing critical support for rapid response to sudden water environment events. In this study, all hyperspectral image preprocessing, feature extraction, and modeling work can be completed on the same day as sampling. The stripe removal method based on median correction achieved good results, even without the use of white balance calibration (Figure 5). The lightweight machine learning model structure is suitable for small-sample datasets, avoiding the complex parameter tuning and overfitting risks typical of deep learning models. Training and thematic mapping can thus be completed rapidly, achieving acceptable fitting accuracy ($R^2$ = 0.768), enabling a true "same-day sampling, same-day mapping" workflow. Furthermore, the constructed model can be directly reused in subsequent monitoring tasks, supporting rapid predictions and long-term applications. In summary, this study not only provides a feasible technical approach for the rapid retrieval of Chl-*a* concentration in water bodies but also offers practical reference for developing an integrated ground–aerial emergency monitoring system.

However, several limitations still exist in this framework. First, although hyperspectral imagery provides abundant spectral information, extracting effective spectral features remains a challenge. While band combinations can effectively capture water quality characteristics, their robustness is limited, and their accuracy varies among different water bodies, leading to inconsistencies across case studies. Traditional models driven by data iteration can identify highly correlated band combinations, yet they are essentially data-driven and lack physical interpretability. Moreover, common spectral preprocessing methods, such as min–max normalization and first-order differential, were not discussed in detail in this study. Future work could focus on discovering more discriminative spectral features or developing novel spectral indices to enhance model input quality.

Second, The availability and data quality of UAV-based hyperspectral imagery remain substantially constrained by environmental conditions and technical limitations. Meteorological factors constitute the primary obstacles to effective data acquisition: rainfall and strong winds can interrupt flight missions, while cloud shadows introduce significant noise into spectral data. Statistical analysis indicates that in 2024, only about half of the days in the study area met the basic flight requirements (no rainfall and wind speeds not exceeding Beaufort scale 3), and only two-thirds of these flyable days offered at least a three-day

favorable weather window (Figure 12). This greatly reduces the temporal availability of UAV-based monitoring. In addition to weather constraints, the subsequent data processing workflow—particularly the image mosaicking stage—also presents substantial challenges. Only one of the UAV images acquired in this study yielded a mosaicking result of acceptable quality due to the limitations of the current mosaicking algorithms. Future research could focus on optimizing or even independently developing mosaicking algorithms to improve image registration and fusion accuracy. Based on this, multi-temporal high-frequency water quality monitoring (e.g., four observation phases within a single day) can be carried out in target areas. With the aid of high-spatial-resolution data, the spatiotemporal heterogeneity in water quality at the hour scale can be analyzed more precisely.

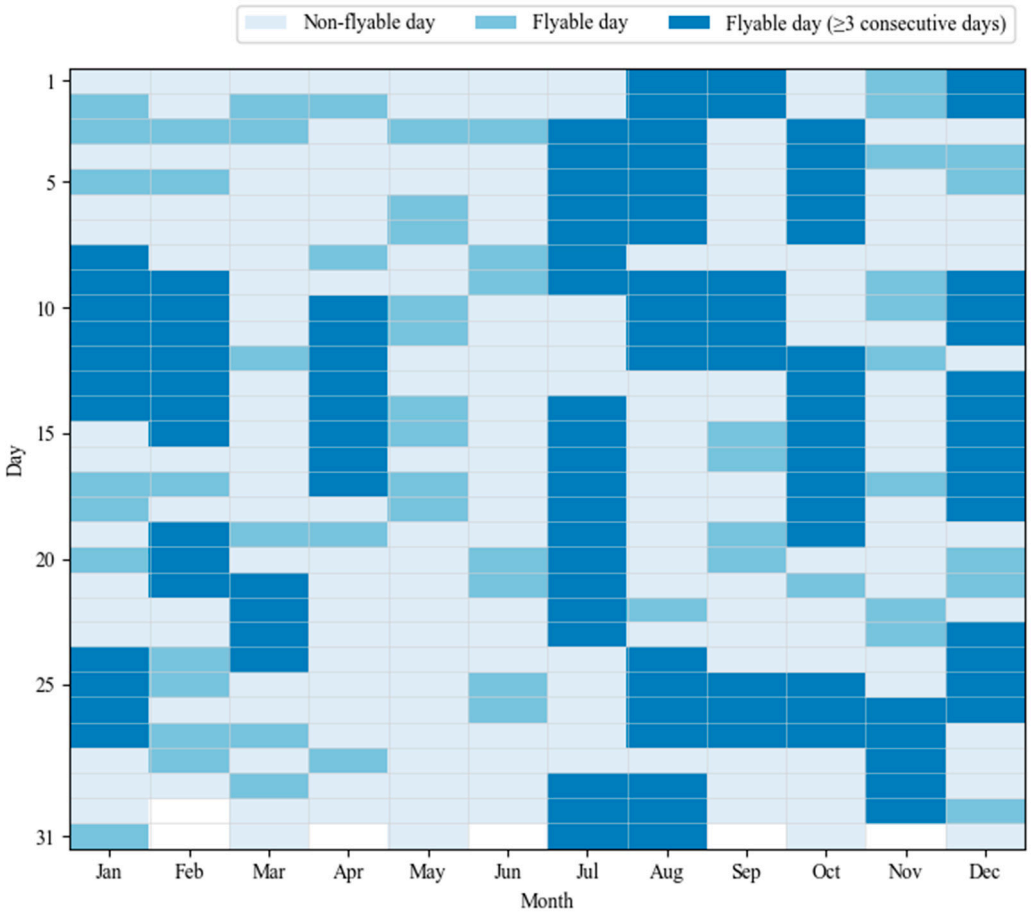


**Figure 12.** Monthly–daily distribution of flyable days and consecutive flight windows in 2024.

Furthermore, developing an integrated, end-to-end processing algorithm is of great significance. Automating the entire workflow—from raw UAV data input to final map generation—would greatly improve the efficiency and consistency of data processing. Finally, this study focuses solely on the retrieval modeling of Chl-*a* concentration. Future research could extend the proposed approach to other key water quality parameters, such as suspended solids, nitrogen, phosphorus, and colored dissolved organic matter. Validation across a wider range of water body types would further assess the applicability and robustness of the proposed technology.

## 5. Conclusions

This study established a UAV–USV collaborative framework, integrated with machine learning, to rapidly estimate Chl-*a* concentrations in a subtropical drinking-water reservoir. Over the course of a three-day intensive campaign, the system successfully collected

30 temporally synchronized UAV–USV sample pairs. Due to the significant short-term variability in Chl-*a* concentrations (CV = 40%), the imaging–sampling time deviations were controlled within 5 min to ensure high temporal consistency.

Preprocessing and feature extraction effectively enhanced the quality of the hyperspectral data. A two-stage band selection procedure identified key spectral combinations centered on the green and red-edge regions, which showed strong correlations with measured Chl-*a* concentrations. Among the four algorithms tested, the RF model demonstrated the best predictive performance and generalization capacity. It achieved an $R^2$ of 0.824 and RMSE of 1.656 μg/L for training, and an $R^2$ of 0.768 and RMSE of 2.111 μg/L for testing. The small performance gap between the training and testing datasets suggests stable behavior, even under limited sample conditions. When applied to UAV imagery, the RF model generated Chl-*a* concentration maps ranging from 5.83 to 16.01 μg/L, which closely aligned with in situ measurements (2–19 μg/L). The spatial patterns revealed the hydrodynamic features of the reservoir, with higher concentrations observed in weakly mixed central zones.

The integrated UAV–USV workflow demonstrated strong operational efficiency, enabling multiple daily observations. It also supported same-day sampling, modeling, and mapping—an essential capability for emergency water-quality assessment. These findings confirm the feasibility and effectiveness of using UAV hyperspectral data, synchronized USV sampling, and lightweight ensemble learning models for rapid Chl-*a* retrieval in small inland water bodies. Future research should focus on improving hyperspectral mosaicking, automating the processing pipeline, and expanding the model's applications to other water-quality parameters and broader temporal-spatial scales. This would enhance the robustness and scalability of the proposed monitoring framework.

**Author Contributions:** Conceptualization, Z.Y. and W.P.; methodology, Z.Y.; software, Z.Y.; validation, L.Q.; investigation, X.C. and L.Q.; data curation, C.L.; writing—original draft preparation, Z.Y.; writing—review and editing, W.P.; visualization, Z.Y.; supervision, W.P.; project administration, W.P.; funding acquisition, W.P. All authors have read and agreed to the published version of the manuscript.

**Funding:** This research was funded by the National Key Research and Development Program of China, grant number 2022YFF1301302-02.

**Data Availability Statement:** The data presented in this study are available on request from the corresponding author due to privacy.

**Acknowledgments:** The authors would like to express their sincere gratitude to the Institute of Urban Environment, Chinese Academy of Sciences, and Fujian Jinjin Water Supply Co., Ltd. (Jinjiang, China) for their valuable assistance with water quality sampling and analysis in this study.

**Conflicts of Interest:** The authors declare no conflicts of interest.

## References

1. Millennium Ecosystem Assessment (MEA). *Ecosystems and Human Well-Being*; Island Press: Washington, DC, USA, 2005; Volume 5.
2. Hestir, E.L.; Brando, V.E.; Bresciani, M.; Giardino, C.; Matta, E.; Villa, P.; Dekker, A.G. Measuring freshwater aquatic ecosystems: The need for a hyperspectral global mapping satellite mission. *Remote Sens. Environ.* **2015**, *167*, 181–195. [CrossRef]
3. Reid, A.J.; Carlson, A.K.; Creed, I.F.; Eliason, E.J.; Gell, P.A.; Johnson, P.T.J.; Kidd, K.A.; MacCormack, T.J.; Olden, J.D.; Ormerod, S.J.; et al. Emerging threats and persistent conservation challenges for freshwater biodiversity. *Biol. Rev.* **2019**, *94*, 849–873. [CrossRef] [PubMed]
4. García-Chicote, J.; Armengol, X.; Rojo, C. Zooplankton abundance: A neglected key element in the evaluation of reservoir water quality. *Limnologica* **2018**, *69*, 46–54. [CrossRef]

5. Paerl, H.W.; Otten, T.G. Harmful Cyanobacterial Blooms: Causes, Consequences, and Controls. *Microb. Ecol.* **2013**, *65*, 995–1010. [CrossRef] [PubMed]
6. Ho, J.C.; Michalak, A.M.; Pahlevan, N. Widespread global increase in intense lake phytoplankton blooms since the 1980s. *Nature* **2019**, *574*, 667–670. [CrossRef]
7. Anderson, D.M.; Glibert, P.M.; Burkholder, J.M. Harmful algal blooms and eutrophication: Nutrient sources, composition, and consequences. *Estuaries* **2002**, *25*, 704–726. [CrossRef]
8. Paerl, H.W.; Barnard, M.A. Mitigating the global expansion of harmful cyanobacterial blooms: Moving targets in a human- and climatically-altered world. *Harmful Algae* **2020**, *96*, 101845. [CrossRef]
9. Stumpf, R.P.; Davis, T.W.; Wynne, T.T.; Graham, J.L.; Loftin, K.A.; Johengen, T.H.; Gossiaux, D.; Palladino, D.; Burtner, A. Challenges for mapping cyanotoxin patterns from remote sensing of cyanobacteria. *Harmful Algae* **2016**, *54*, 160–173. [CrossRef]
10. Ngwenya, N.; Bangira, T.; Sibanda, M.; Gurmessa, S.K.; Mabhaudhi, T. UAV-based remote sensing of chlorophyll-a concentrations in inland water bodies: A systematic review. *Geocarto Int.* **2025**, *40*, 2452246. [CrossRef]
11. Gui, J.; Sun, J. Phytoplankton carbon to chlorophyll a model development: A review. *Front. Mar. Sci.* **2024**, *11*, 1466072. [CrossRef]
12. Brivio, P.A.; Giardino, C.; Zilioli, E. Validation of satellite data for quality assurance in lake monitoring applications. *Sci. Total Environ.* **2001**, *268*, 3–18. [CrossRef] [PubMed]
13. Schaeffer, B.A.; Schaeffer, K.G.; Keith, D.; Lunetta, R.S.; Conmy, R.; Gould, R.W. Barriers to adopting satellite remote sensing for water quality management. *Int. J. Remote Sens.* **2013**, *34*, 7534–7544. [CrossRef]
14. Shi, K.; Zhang, Y.L.; Zhu, G.W.; Qin, B.Q.; Pan, D.L. Deteriorating water clarity in shallow waters: Evidence from long term MODIS and in-situ observations. *Int. J. Appl. Earth Obs. Geoinf.* **2018**, *68*, 287–297. [CrossRef]
15. Dalu, T.; Muthivhi, F.; Dondofema, F.; Munyai, L.; Mpopetsi, P.; Dube, T.; Wu, N.C. Understanding the Spatiotemporal Variation of Water Quality and Phytoplankton Biomass in Subtropical Reservoir Using the Blue-Sky Multispectral Data. *Ecohydrology* **2025**, *18*, e70070. [CrossRef]
16. Chen, J.Y.; Chen, S.S.; Fu, R.; Li, D.; Jiang, H.; Wang, C.Y.; Peng, Y.S.; Jia, K.; Hicks, B.J. Remote Sensing Big Data for Water Environment Monitoring: Current Status, Challenges, and Future Prospects. *Earth's Future* **2022**, *10*, e2021EF002289. [CrossRef]
17. Wang, W.J.; Shi, K.; Zhang, Y.B.; Li, N.; Sun, X.; Zhang, D.; Zhang, Y.L.; Qin, B.Q.; Zhu, G.W. A ground-based remote sensing system for high-frequency and real-time monitoring of phytoplankton blooms. *J. Hazard. Mater.* **2022**, *439*, 129623. [CrossRef]
18. Lee, H.S.; Lee, J.H.W. Continuous Monitoring of Short Term Dissolved Oxygen and Algal Dynamics. *Water Res.* **1995**, *29*, 2789–2796. [CrossRef]
19. Cao, Z.G.; Ma, R.H.; Melack, J.M.; Duan, H.T.; Liu, M.; Kutser, T.; Xue, K.; Shen, M.; Qi, T.C.; Yuan, H.L. Landsat observations of chlorophyll-a variations in Lake Taihu from 1984 to 2019. *Int. J. Appl. Earth Obs. Geoinf.* **2022**, *106*, 102642. [CrossRef]
20. Cheng, K.H.; Chan, S.N.; Lee, J.H.W. Remote sensing of coastal algal blooms using unmanned aerial vehicles (UAVs). *Mar. Pollut. Bull.* **2020**, *152*, 110889. [CrossRef]
21. Giardino, C.; Brando, V.E.; Gege, P.; Pinnel, N.; Hochberg, E.; Knaeps, E.; Reusen, I.; Doerffer, R.; Bresciani, M.; Braga, F.; et al. Imaging Spectrometry of Inland and Coastal Waters: State of the Art, Achievements and Perspectives. *Surv. Geophys.* **2019**, *40*, 401–429. [CrossRef]
22. Meng, X.; Shen, H.; Zhang, L.; Yuan, Q.; Li, H. A unified framework for spatio-temporal-spectral fusion of remote sensing images. In Proceedings of the 2015 IEEE International Geoscience and Remote Sensing Symposium (IGARSS), Milan, Italy, 26–31 July 2015; pp. 2584–2587.
23. Wu, D.; Li, R.P.; Zhang, F.Y.; Liu, J. A review on drone-based harmful algae blooms monitoring. *Environ. Monit. Assess.* **2019**, *191*, 211. [CrossRef] [PubMed]
24. Sibanda, M.; Mutanga, O.; Chimonyo, V.G.P.; Clulow, A.D.; Shoko, C.; Mazvimavi, D.; Dube, T.; Mabhaudhi, T. Application of Drone Technologies in Surface Water Resources Monitoring and Assessment: A Systematic Review of Progress, Challenges, and Opportunities in the Global South. *Drones* **2021**, *5*, 84. [CrossRef]
25. Mishra, V.; Avtar, R.; Prathiba, A.P.; Mishra, P.K.; Tiwari, A.; Sharma, S.K.; Singh, C.H.; Yadav, B.C.; Jain, K. Uncrewed Aerial Systems in Water Resource Management and Monitoring: A Review of Sensors, Applications, Software, and Issues. *Adv. Civ. Eng.* **2023**, *2023*, 3544724. [CrossRef]
26. Kislik, C.; Dronova, I.; Kelly, M. UAVs in Support of Algal Bloom Research: A Review of Current Applications and Future Opportunities. *Drones* **2018**, *2*, 35. [CrossRef]
27. Byrd, K.; Wu, J.Y.; Lee, J.Y. Harmful Algal Bloom Monitoring with Unmanned Aerial Vehicles: Tools, Challenges, and Public Health Implications. *Toxins* **2025**, *17*, 475. [CrossRef]
28. Kudela, R.M.; Palacios, S.L.; Austerberry, D.C.; Accorsi, E.K.; Guild, L.S.; Torres-Perez, J. Application of hyperspectral remote sensing to cyanobacterial blooms in inland waters. *Remote Sens. Environ.* **2015**, *167*, 196–205. [CrossRef]
29. Seo, S.H.; Choi, J.I.; Song, J. Secure Utilization of Beacons and UAVs in Emergency Response Systems for Building Fire Hazard. *Sensors* **2017**, *17*, 2200. [CrossRef]

30. Lu, M.; Liao, X.H.; Yue, H.Y.; Huang, Y.H.; Ye, H.P.; Xu, C.C.; Huang, S.F. Optimizing distribution of droneports for emergency monitoring of flood disasters in China. *J. Flood Risk Manag.* **2020**, *13*, e12593. [CrossRef]
31. Maciel, D.A.; Barbosa, C.C.F.; Novo, E.; Flores, R., Jr.; Begliomini, F.N. Water clarity in Brazilian water assessed using Sentinel-2 and machine learning methods. *ISPRS J. Photogramm. Remote Sens.* **2021**, *182*, 134–152. [CrossRef]
32. Rubin, H.J.; Lutz, D.A.; Steele, B.G.; Cottingham, K.L.; Weathers, K.C.; Ducey, M.J.; Palace, M.; Johnson, K.M.; Chipman, J.W. Remote Sensing of Lake Water Clarity: Performance and Transferability of Both Historical Algorithms and Machine Learning. *Remote Sens.* **2021**, *13*, 1434. [CrossRef]
33. Wang, Z.M.; Kawamura, K.; Sakuno, Y.J.; Fan, X.Y.; Gong, Z.; Lim, J.Y. Retrieval of Chlorophyll-a and Total Suspended Solids Using Iterative Stepwise Elimination Partial Least Squares (ISE-PLS) Regression Based on Field Hyperspectral Measurements in Irrigation Ponds in Higashihiroshima, Japan. *Remote Sens.* **2017**, *9*, 264. [CrossRef]
34. Hafeez, S.; Wong, M.S.; Ho, H.C.; Nazeer, M.; Nichol, J.; Abbas, S.; Tang, D.L.; Lee, K.H.; Pun, L.L. Comparison of Machine Learning Algorithms for Retrieval of Water Quality Indicators in Case-II Waters: A Case Study of Hong Kong. *Remote Sens.* **2019**, *11*, 617. [CrossRef]
35. Xiao, Y.; Li, X.R.; Chen, J.H.; Guo, S.H.; Xu, Y.; Nie, X.Y.; Nie, Y.J.; Hao, F.H.; Fu, Y.S. A novel approach for tracking the diurnal dynamics of chlorophyll-a in lakes using UAV hyperspectral images. *J. Hydrol.* **2025**, *660*, 133403. [CrossRef]
36. Zhang, Y.S.; Wu, L.; Ren, H.Z.; Deng, L.C.; Zhang, P.C. Retrieval of Water Quality Parameters from Hyperspectral Images Using Hybrid Bayesian Probabilistic Neural Network. *Remote Sens.* **2020**, *12*, 1567. [CrossRef]
37. Petch, J.; Di, S.; Nelson, W. Opening the Black Box: The Promise and Limitations of Explainable Machine Learning in Cardiology. *Can. J. Cardiol.* **2022**, *38*, 204–213. [CrossRef]
38. Rocha, A.D.; Groen, T.A.; Skidmore, A.K.; Darvishzadeh, R.; Willemen, L. The Naive Overfitting Index Selection (NOIS): A new method to optimize model complexity for hyperspectral data. *ISPRS J. Photogramm. Remote Sens.* **2017**, *133*, 61–74. [CrossRef]
39. Trinh, H.; Kieu, H.T.; Pak, H.Y.; Pang, D.S.C.; Cokro, A.A.; Law, A.W.K. A Framework for Survey Planning Using Portable Unmanned Aerial Vehicles (pUAVs) in Coastal Hydro-Environment. *Remote Sens.* **2022**, *14*, 2283. [CrossRef]
40. Ritchie, R.J. Consistent sets of spectrophotometric chlorophyll equations for acetone, methanol and ethanol solvents. *Photosynth. Res.* **2006**, *89*, 27–41. [CrossRef]
41. Pak, H.Y.; Kieu, H.T.; Lin, W.S.; Khoo, E.; Law, A.W.K. CoastalWQL: An Open-Source Tool for Drone-Based Mapping of Coastal Turbidity Using Push Broom Hyperspectral Imagery. *Remote Sens.* **2024**, *16*, 708. [CrossRef]
42. Pölönen, I.; Puupponen, H.-H.; Honkavaara, E.; Lindfors, A.; Saari, H.; Markelin, L.; Hakala, T.; Nurminen, K. UAV-based hyperspectral monitoring of small freshwater area. In Proceedings of the Remote Sensing for Agriculture, Ecosystems, and Hydrology XVI, Amsterdam, The Netherlands, 23–25 September 2014; pp. 331–339.
43. Shang, S.L.; Lee, Z.P.; Lin, G.; Hu, C.M.; Shi, L.H.; Zhang, Y.N.A.; Li, X.D.; Wu, J.Y.; Yan, J. Sensing an intense phytoplankton bloom in the western Taiwan Strait from radiometric measurements on a UAV. *Remote Sens. Environ.* **2017**, *198*, 85–94. [CrossRef]
44. Werther, M.; Odermatt, D.; Simis, S.G.H.; Gurlin, D.; Jorge, D.S.F.; Loisel, H.; Hunter, P.D.; Tyler, A.N.; Spyrakos, E. Characterising retrieval uncertainty of chlorophyll-a algorithms in oligotrophic and mesotrophic lakes and reservoirs. *ISPRS J. Photogramm. Remote Sens.* **2022**, *190*, 279–300. [CrossRef]
45. Zeng, Y.L.; Hao, D.L.; Huete, A.; Dechant, B.; Berry, J.; Chen, J.M.; Joiner, J.; Frankenberg, C.; Bond-Lamberty, B.; Ryu, Y.; et al. Optical vegetation indices for monitoring terrestrial ecosystems globally. *Nat. Rev. Earth Environ.* **2022**, *3*, 477–493. [CrossRef]
46. Gitelson, A.A.; Dall'Olmo, G.; Moses, W.; Rundquist, D.C.; Barrow, T.; Fisher, T.R.; Gurlin, D.; Holz, J. A simple semi-analytical model for remote estimation of chlorophyll-a in turbid waters: Validation. *Remote Sens. Environ.* **2008**, *112*, 3582–3593. [CrossRef]
47. Mishra, S.; Mishra, D.R. Normalized difference chlorophyll index: A novel model for remote estimation of chlorophyll-a concentration in turbid productive waters. *Remote Sens. Environ.* **2012**, *117*, 394–406. [CrossRef]
48. Yang, W.; Matsushita, B.; Chen, J.; Fukushima, T.; Ma, R.H. An Enhanced Three-Band Index for Estimating Chlorophyll-a in Turbid Case-II Waters: Case Studies of Lake Kasumigaura, Japan, and Lake Dianchi, China. *IEEE Geosci. Remote Sens. Lett.* **2010**, *7*, 655–659. [CrossRef]
49. Kneubühler, M.; Frank, T.; Kellenberger, T.; Pasche, N.; Schmid, M.; Lacoste, H.; Ouwehand, L. Mapping chlorophyll-a in Lake Kivu with remote sensing methods. In Proceedings of the Envisat Symposium 2007, Montreux, Switzerland, 23–27 April 2007.
50. Gilerson, A.A.; Gitelson, A.A.; Zhou, J.; Gurlin, D.; Moses, W.; Ioannou, I.; Ahmed, S.A. Algorithms for remote estimation of chlorophyll-a in coastal and inland waters using red and near infrared bands. *Opt. Express* **2010**, *18*, 24109–24125. [CrossRef]
51. Le, C.F.; Li, Y.M.; Zha, Y.; Sun, D.Y.; Huang, C.C.; Lu, H. A four-band semi-analytical model for estimating chlorophyll a in highly turbid lakes: The case of Taihu Lake, China. *Remote Sens. Environ.* **2009**, *113*, 1175–1182. [CrossRef]
52. Xu, F.X.; Gao, Z.Q.; Jiang, X.P.; Shang, W.T.; Ning, J.C.; Song, D.B.; Ai, J.Q. A UAV and S2A data-based estimation of the initial biomass of green algae in the South Yellow Sea. *Mar. Pollut. Bull.* **2018**, *128*, 408–414. [CrossRef]
53. Alawadi, F. Detection of surface algal blooms using the newly developed algorithm surface algal bloom index (SABI). In Proceedings of the Remote Sensing of the Ocean, Sea Ice, and Large Water Regions 2010, Toulouse, France, 20–23 September 2010; pp. 45–58.

54. Liu, B.; Li, T.H. A Machine-Learning-Based Framework for Retrieving Water Quality Parameters in Urban Rivers Using UAV Hyperspectral Images. *Remote Sens.* **2024**, *16*, 905. [CrossRef]
55. Coelho, F.; Braga, A.P.; Verleysen, M. Multi-objective semi-supervised feature selection and model selection based on Pearson's correlation coefficient. In Proceedings of the Iberoamerican Congress on Pattern Recognition, São Paulo, Brazil, 8–11 November 2010; pp. 509–516.
56. Speybroeck, N. Classification and regression trees. *Int. J. Public Health* **2012**, *57*, 243–246. [CrossRef]
57. Pak, H.Y.; Law, A.W.K.; Lin, W.S.; Khoo, E. Sun Glint-Aware Restoration (SUGAR): A robust sun glint correction algorithm for UAV imagery to enhance monitoring of turbid coastal environments. *Environ. Monit. Assess.* **2025**, *197*, 254. [CrossRef]
58. Zhang, Y.Z.; Zhang, T.X. Structure-guided unidirectional variation de-striping in the infrared bands of MODIS and hyperspectral images. *Infrared Phys. Technol.* **2016**, *77*, 132–143. [CrossRef]
59. Qiu, Y.G.; Huang, J.C.; Luo, J.H.; Xiao, Q.T.; Shen, M.; Xiao, P.F.; Peng, Z.L.; Jiao, Y.Q.; Duan, H.T. Monitoring, simulation and early warning of cyanobacterial harmful algal blooms: An upgraded framework for eutrophic lakes. *Environ. Res.* **2025**, *264*, 120296. [CrossRef]


**Disclaimer/Publisher's Note:** The statements, opinions and data contained in all publications are solely those of the individual author(s) and contributor(s) and not of MDPI and/or the editor(s). MDPI and/or the editor(s) disclaim responsibility for any injury to people or property resulting from any ideas, methods, instructions or products referred to in the content.